Effect of annealing temperature on the microstructure evolution, mechanical and wear behavior of NiCr–WC–Co HVOF-sprayed coatings

Azzeddine Mazouzi[1], Boubekeur Djerdjare[1], Salim Triaa[1], Amine Rezzoug[2], Billel Cheniti[2], Samir M. Aouadi[3,a)]

[1]*Laboratoire des Sciences et Génie des Matériaux (LSGM), Faculté de Génie Mécanique et du Génie des Procédés, Université des Sciences et de la Technologie Houari Boumediene, 16111 Bab-Ezzouar, Algiers, Algeria*
[2]*Research Center in Industrial Technologies (CRTI), 16014 Cheraga, Algeria*
[3]*Department of Materials Science and Engineering, University of North Texas, Denton, Texas 76207, USA*
[a)]Address all correspondence to this author. e-mail: samir.aouadi@unt.edu

In the present work, the effect of annealing temperature on the microstructure, mechanical and tribological properties of NiCr–WC–Co coatings produced by the high-velocity oxy-fuel (HVOF) technique has been investigated. X-ray diffraction and scanning electron microscopy revealed the dissolution of WC into the NiCr matrix to form W_2C and Cr_3C_2 with the annealing process. This dissolution became complete at 800 °C. The mechanical properties of the coatings were investigated using nano-indentation and Vickers fracture toughness measurements. These measurements suggested that the hardness, Young's modulus, and fracture toughness values increased because of the newly formed carbide phases as a result of the dissolution of the WC particles. The overall properties of the coatings were found to be optimum for annealing temperatures of 800 °C. The wear mechanism appears to be abrasive in the as-sprayed coating, and it becomes a combination of an abrasive and oxidative wear with increasing the annealing temperature.

Introduction

In the last three decades, the high-velocity oxy-fuel (HVOF) spraying technique has been used in a wide range of applications with an emphasis on the production of hard coatings (i.e., WC–Co, NiCr, and Cr_xC_y) since it is a relatively low-cost process for the production of dense coatings with relatively high bonding strength [1, 2, 3]. An emerging class of hard coatings produced using this technique are metal matrix composites (MMCs) which consist of a metal matrix that is reinforced with ceramic particles [4]. MMCs were shown to perform better than their single-phase counterparts by providing high (i) hardness, (ii) fracture toughness, and (iii) abrasion and erosion resistance even at high temperatures [4]. The addition of hard particles also enhances coating cohesion by developing micro-asperities that promote bonding, further lowering porosity and increasing density of the HVOF-sprayed coatings [4]. MMCs that consist of WC or Cr_2C_3 particles in a Ni-based matrix have been produced using HVOF and are currently used to protect turbine engine components and heat exchangers in power generation systems where thermal shock resistance and increased toughness are required [5].

A potential disadvantage of using HVOF to manufacture hard coatings is that they are known to have inherent defects that include cracks, porosity, residual stresses, oxidation of particles, and the presence of unmolten particles in the coatings. In addition, the heat input generated during thermal spray operations significantly affects the microstructure of these composites resulting in particle dissolution and the formation of a metastable structure [6, 7, 8]. All of the above defects have an adverse effect on the overall mechanical and tribological properties of the coatings [9, 10, 11]. Post-processing annealing of this class of materials was successfully used to significantly decrease the density of these defects [12, 13]. The employment of an adequate annealing treatment was found to be beneficial in relaxing thermal stresses induced by the thermal spray operation and to improve the mechanical response of the coatings.

Recently, numerous researchers investigated the direct effect of heat treatment on the overall properties of sprayed

coatings. It is known that an annealing treatment alters the structure of a material by causing important changes to its microstructure and chemistry which, in turn, affects its properties such as strength, ductility, and hardness. For thermally sprayed coatings, annealing is usually carried out at elevated temperatures, but well below the coating melting temperature [14]. Guo et al. [15] investigated the annealing strengthening effect of Fe5Cr5Co5SiTiNbMoW high-entropy alloy coatings and discovered that the microstructure changed significantly above 850 °C leading to enhanced mechanical properties. Zhang and co-workers [16] studied the effect of heat treatment on the structure and property evolution of NiCrBSi coatings deposited using the atmospheric plasma spray process. They reported that post-processing annealing enhanced coating crystallinity and hardness but failed to improve wear properties. Hence, Bergant et al. [17] demonstrated that the adhesion of flame-sprayed NiCrBSi coatings was substantially enhanced after a 930 °C heat treatment. Moreover, denser NiCr coatings with a homogeneous microstructure, a low porosity, and low residual stresses were achieved by a five-minute re-melting treatment [17, 18]. In another study, Lua et al. [19] prepared Ni60/h-BN MMC coatings using laser cladding and concluded that both hardness and wear properties were improved after annealing. Similarly, Shipway and co-workers [20] found that heat treatment improved the wear behavior of HVOF-sprayed WC–17Co coatings. Asl et al. [21, 22] reported that annealing treatments changed the wear mechanisms from cutting to gouging abrasion in WC–17Co HVOF coatings. The dissolution of carbides in the metallic matrix during thermal spraying was found to significantly influence coatings' microstructural stability [23]. The heat treatment of these coatings caused the precipitation of secondary carbides within the supersaturated metallic matrix and increased the effective carbide volume fraction leading to significant changes to the composition and microstructure of the matrix [23]. In a different study, Janka et al. [12] studied the influence of heat treatment on the abrasive wear resistance of Ni–Cr–Cr_3C_2 composite coating deposited by the HVOF spray process. They found that heat treatment reduces the ductility of the metallic matrix. More specifically, they reported that thermal spray followed by the heat treatment of NiCr–Cr_3C_2 powder caused dissolution of the carbide particles and increased the carbon and chromium content in the molten NiCr matrix, while small particles underwent rapid cooling and solidification resulting in a supersaturated metallic matrix [24]. They concluded that the as-deposited thermodynamically metastable coating became much more stable as a result of the annealing process.

In this study, the authors report a study on the relationship between post-processing heat treatment, structure evolution, and the mechanical properties of HVOF NiCr–WC10Co MMCs. WC particles were used as reinforcing particles in these MMCs due to their high hardness, strength, and fracture toughness compared to other carbides or oxides [4]. The metallic matrix (NiCr–Co) was selected because of its excellent adhesion to the substrate, its superior corrosion protection, and its compatibility with WC [25]. The focus will be to investigate the influence of different annealing treatments (700, 800, and 900 °C) on the microstructural changes of the coatings, which will then be correlated to their hardness, interfacial adhesion, and tribological performance (wear rate and wear mechanisms). Optimum post-processing heat treatment conditions will be suggested for this class of materials.

Results

Surface coating and interface structure

Figure 1 shows the X-ray diffraction (XRD) patterns for as-sprayed and annealed NiCr–WC10Co4Cr coatings. The patterns revealed the presence of WC, W_2C, and NiCr phases in the as-sprayed coatings. In addition, two very broad peaks from 15° to 25° and from 38° to 52° were observed and may be attributed to the differential dissolution of the carbides in the NiCr matrix and to the presence of partially amorphous/ fine crystalline phases [23]. The XRD patterns of the annealed samples revealed the presence of peaks that correspond to the initial post-deposition phases, i.e., WC, W_2C, and NiCr, in addition to new peaks that formed as a result of the annealing process. The newly formed phases were identified as carbide (Cr_3C_2 and $Cr_{23}C_6$) and oxide (NiO_4W and Cr_2O_3) phases. These results suggest that annealing caused the dissolution/de-carburization of WC and the formation of chromium carbide phases. Carrying out the heat treatment in air also lead to the formation of chromium- and tungsten-based oxide phases. Cr_2O_3 and $CoWO_4$ have been reported in the literature as effective lubricants due to their high ionic potential and would be beneficial in reducing friction during sliding [26]. The XRD patterns for samples annealed at higher temperatures (900 °C) indicated a decrease in the intensity of the WC peak and an increase in the intensity of the oxide phases. The ratio of the intensity of the oxide phases may have an important role to play in the wear behavior of oxidized WC–Co systems coatings, as reported in Ref. [27].

Figures 2(a)–2(d) show optical micrographs of as-sprayed and annealed NiCr–WC–Co coatings on stainless steel coupons. The selected annealing temperatures were 700, 800, and 900 °C. These figures suggested that the NiCr–WC–Co coatings had a uniform thickness of ~300 μm. At this scale, porosity was observed in all samples, but no cracks or delamination were detected. The volume percent of porosity was found to decrease with an increase in annealing temperature with values of 2.50 ± 0.02, 2.30 ± 0.02, 1.76 ± 0.02, and $1.60 \pm$
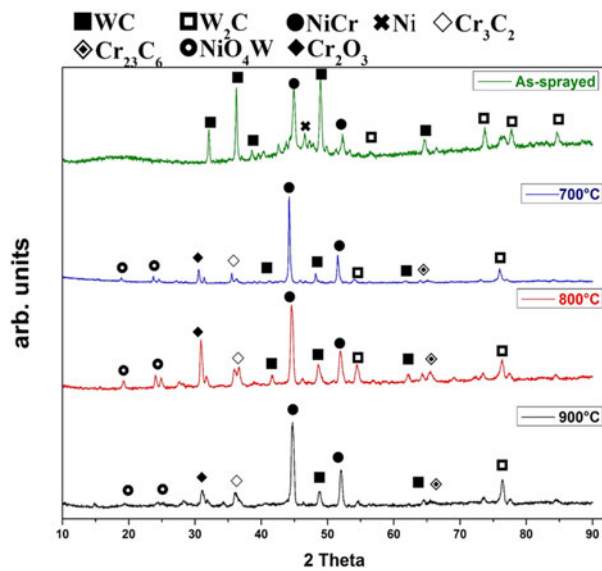
Figure 1: XRD patterns for as-sprayed and annealed coatings NiCr–WC10Co4Cr coatings.

0.02 for as-sprayed, and annealed samples at 700, 800, and 900 °C, respectively.

The scanning electron microscropy (SEM) images of the coatings, illustrated in Figs. 2(e) and 2(f), indicated that after HVOF operation, the original spherical shape of the WC particles changed and transformed into splat-like structures due to the important plastic deformation induced during their impact

upon the steel substrate, which was a result of the high particle velocity and working temperature. Furthermore, the typical lamellar structure of the metallic matrix combined with the partial dissolution of Cr [21] was observed in the as-sprayed coating. This dissolution is enhanced by the increase in temperature and becomes complete at 800 °C [Fig. 2(f)]. Hence, the higher the annealing temperature, the greater the extent of WC particles dissolution. In addition, the excess carbon that results from the WC dissolution diffuses into the metallic matrix and forms another carbide phase ($Cr_{23}C_6$) and new eutectic phases such as W_2C and W_4Ni. It is reported by Liyanage et al. [28] that Cr content increases the dissolution of WC particles and promotes the formation of $Cr_7W_3C_6$ secondary carbide in the metallic matrix, in good agreement with the results shown in Fig. 3. In Figs. 3(a) and 3(b), the formation of a dendritic structure was observed. Energy-dispersive X-ray spectroscopy (EDS) analysis (Table 1) of this dendritic phase revealed a high concentration of W (7.3 wt%) and a low concentration of the inter-dendritic phase (5.1 wt%). The formation of a dendritic structure can be explained as follows [29, 30]: since the melting temperature of W is much higher than that of Ni and Cr, solidification initially promotes the nucleation of W during the cooling process and allows the formation of a W-rich dendritic phase. During the cooling process, elemental Ni and Cr remain trapped in the inter-dendritic space due to the decrease in temperature, which results in an overall slow diffusion rate. Hence, carbides are formed in the
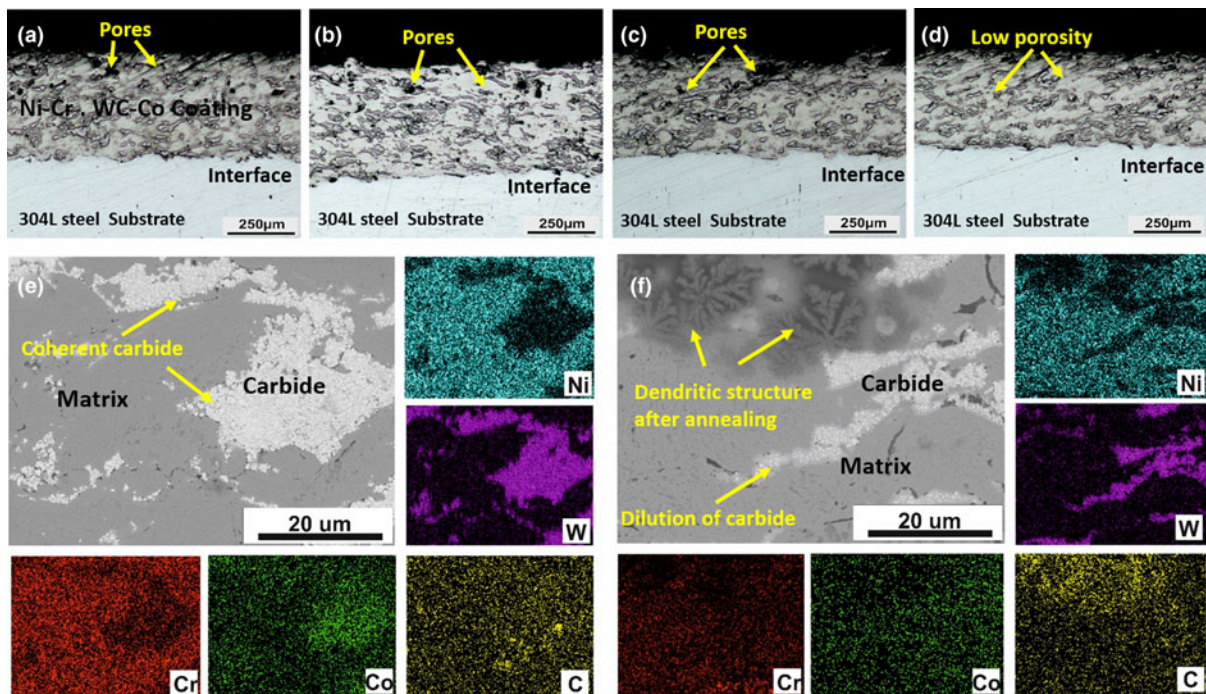

Figure 2: Cross-sectional optical micrographs for (a) as-sprayed and annealed samples at (b) 700 °C, (c) 800 °C, and (d) 900 °C. (e and f) Cross-sectional SEM micrographs and the corresponding elemental maps before and after annealing at 800 °C.
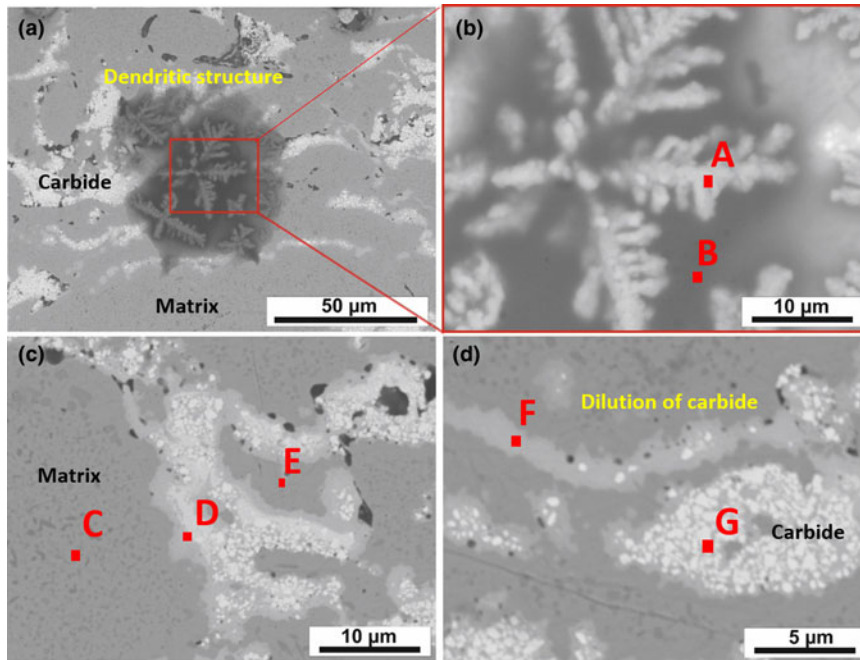
Figure 3: (a and b) Micrographs illustrating the dendritic structure in the binder matrix after annealing at 800 °C. (c and d) SEM cross-sectional micrograph of the dilution of carbide after annealing at 800 °C.

TABLE 1: EDS analyses for Points A, B, C, D, E, F, and G illustrated in Fig. 3.

Powders (wt%)	W	Ni	Cr	Co	C	Fe
A	07.25	37.14	09.99	01.21	33.38	11.03
B	05.14	39.89	34.87	01.40	02.93	05.78
C	11.13	63.83	08.16	1.76	10.32	04.89
D	37.25	27.50	17.14	1.73	13.33	03.05
E	25.68	40.64	10.70	03.05	10.72	03.00
F	39.89	05.14	34.87	01.40	12.93	05.78
G	61.25	00.97	05.40	13.18	17.09	1.85

metallic matrix upon annealing. The amount of these carbide keeps increasing with an increase in the annealing temperature and is accompanied by a significant increase in the dissolution of WC particles in the matrix. EDS analysis of the carbide phases in the samples annealed at 800 °C [Figs. 3(c) and 3 (d)] revealed that the concentration of W decreased drastically from 61 to 40 wt% (Table 1—Points F and G) suggesting the dissolution of WC particles due to the high solubility limit of W in Ni (∼9%) at these temperatures, in agreement with the W–Ni binary phase diagram [31, 32]. Therefore, the amount of WC decarburized in the matrix depends on the selected annealing temperature.

Effect of annealing temperature on the mechanical behavior of the coatings

Figures 4(a)–4(c) show the load–displacement curves for as-sprayed and annealed samples measured at three different locations: (i) on the WC ceramic particles, (ii) on the metallic matrix (NiCr–Co), and (iii) at the ceramic–metal interface. As

expected, the maximum penetration depth was greater for the metallic matrix [Fig. 4(a)] than for the WC particles [Fig. 4 (c)]. Furthermore, the slopes of the unloading segments of the WC particles are steeper than those measured for the metallic matrix and the interfaces, indicating higher stiffness values for the WC particles. The corresponding hardness (H_{IT}) and elastic modulus (E_{IT}) values for each of the sample areas were calculated using the Oliver and Pharr method [33] and are summarized in Table 2. It is clear that regardless of the annealing temperature, the recorded values for H_{IT} and E_{IT} did not vary much for the WC particles (on average ∼ $H_{IT} = 35 \pm 2$ GPa and $E_{IT} = 410 \pm 30$ GPa). The annealing treatment resulted in an increase in the hardness and elastic modulus values of the metallic matrix from $H_{IT} = 5 \pm 1$ GPa and $E_{IT} = 132 \pm 9$ GPa for the as-sprayed to 10 ± 2 GPa and 240 ± 20 GPa for samples annealed at 700 °C, respectively. The hardness values of the matrix for samples reached the highest values for samples annealed at 900 °C. The increase in hardness and Young's modulus values correlates with the metallic matrix hardening that results from the dissolution of hard compounds (small WC particles) into the matrix and the formation of binary (Cr_3C_6) and ternary (W–C–Cr) carbides with an increase in the annealing temperature, as discussed in the "Surface coating and interface structure" section. However, the observed decrease in hardness at 800 °C is hypothesized to correspond to the dissolution of a large amount of these carbides into the matrix due to the heating process. The increase in the metallic matrix hardness is accompanied by a decrease in the volume fraction of the WC particles. The hardness remains roughly unchanged at the WC particle–metal matrix interfaces,
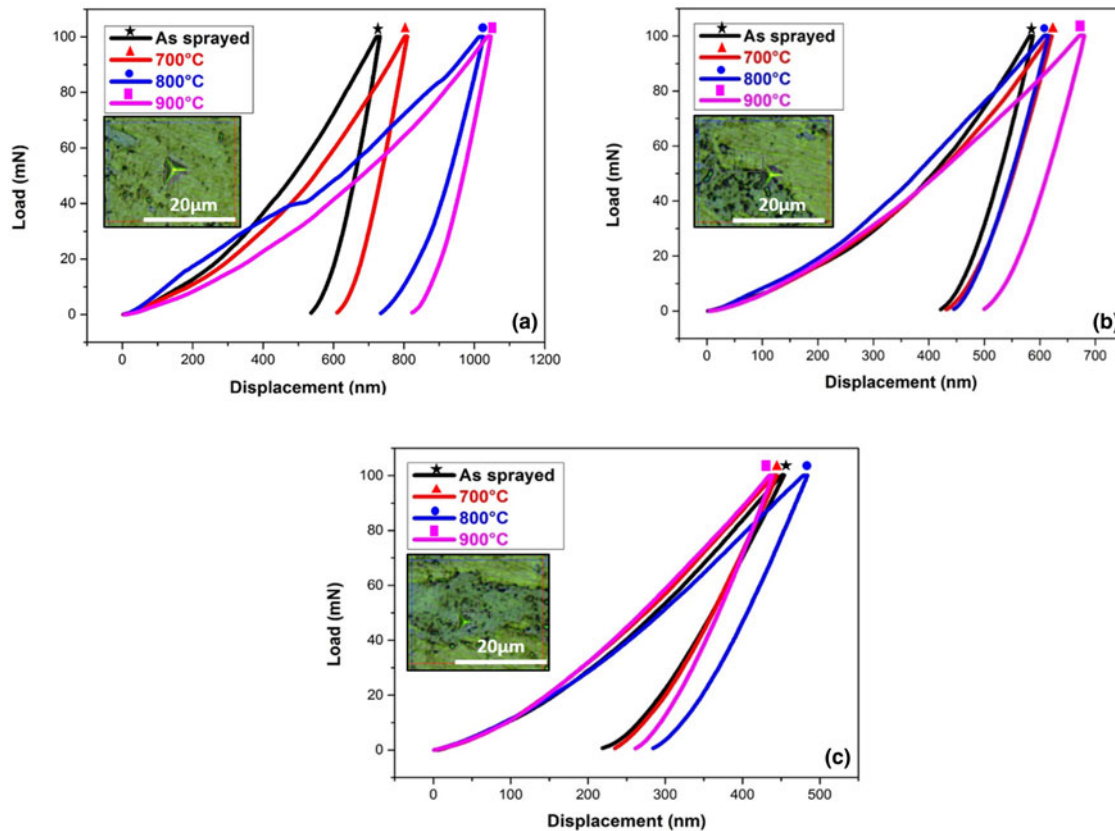
Figure 4: Load–displacement curves using 100 mN load for (a) binder matrix, (b) the interface (binder matrix + carbide), and (c) the carbide phase.

TABLE 2: Hardness and Young's modulus distributions.

	Hardness H (GPa)/ Young's modulus E (GPa)	As-sprayed	700 °C	800 °C	900 °C
Binder matrix	H	05 ± 1	08 ± 1	06 ± 1	10 ± 2
	E	132 ± 10	195 ± 6	212 ± 11	241 ± 18
Interface matrix–carbide	H	15 ± 3	15 ± 2	16 ± 2	14 ± 3
	E	302 ± 15	299 ± 22	326 ± 32	311 ± 13
Carbide	H	34 ± 4	33 ± 6	36 ± 3	36 ± 5
	E	390 ± 32	387 ± 43	427 ± 52	422 ± 30
Coating	$(E/H)_C$	15.21	15.59	16.58	16.09
	$(H/E)_C$	0.065	0.054	0.060	0.062
Substrate	H	1.65 ± 0.4	1.73 ± 0.4	1.70 ± 0.3	1.63 ± 0.4
	E	205 ± 07	210 ± 17	207 ± 09	213 ± 21
	$(E/H)_s$	122.02	121.38	121.76	130.67
Substrate/ Coating	$(E/H)_i^{1/2}$	**9.394**	**9.398**	**9.444**	**9.765**

except for the samples that were heat-treated at 800 °C for which the largest values were recorded.

Figure 5(a) shows schematic highlighting fundamental principles of an interfacial indentation test used to quantify the cohesive energy of the annealed coatings and Fig. 5(b) shows graphs of interfacial fracture toughness and coating hardness values as a function of temperature, and optical images coatings annealed at 900 and 700 °C in Figs. 5(c) and 5(d), respectively. Figure 5(b) indicates that the as-sprayed coatings exhibited a low hardness (470 HV01), which was attributed to the high porosity levels that result from the HVOF thermal spray process. Coatings annealed at 700 °C displayed the largest hardness values (625 HV01), which may be explained by the dissolution of the WC particles and the formation of chromium carbide at these temperatures. Lower hardness values were recorded for samples annealed at 800 and 900 °C, respectively. The decarburization of WC particles is the main factor that affects coating hardness. To quantify the cohesive energy of the annealed coatings, the interfacial fracture toughness was evaluated using Vickers indents at the interface. The evolution of the average toughness values (K_{IC}) as a function of annealing temperatures is also illustrated in Fig. 5(b). The fracture toughness for samples annealed at 700 °C is lower than that of the as-sprayed ones and reached the highest values for samples annealed at 900 °C. In addition, the crack length at the substrate-coating interface was the shortest for the samples annealed at 900 °C, as shown in Figs. 5(c) and 5(d). This behavior may be attributed to the corresponding coating hardness. For the samples annealed at 700 °C, the hardness reached a maximum value because of the thermal stresses
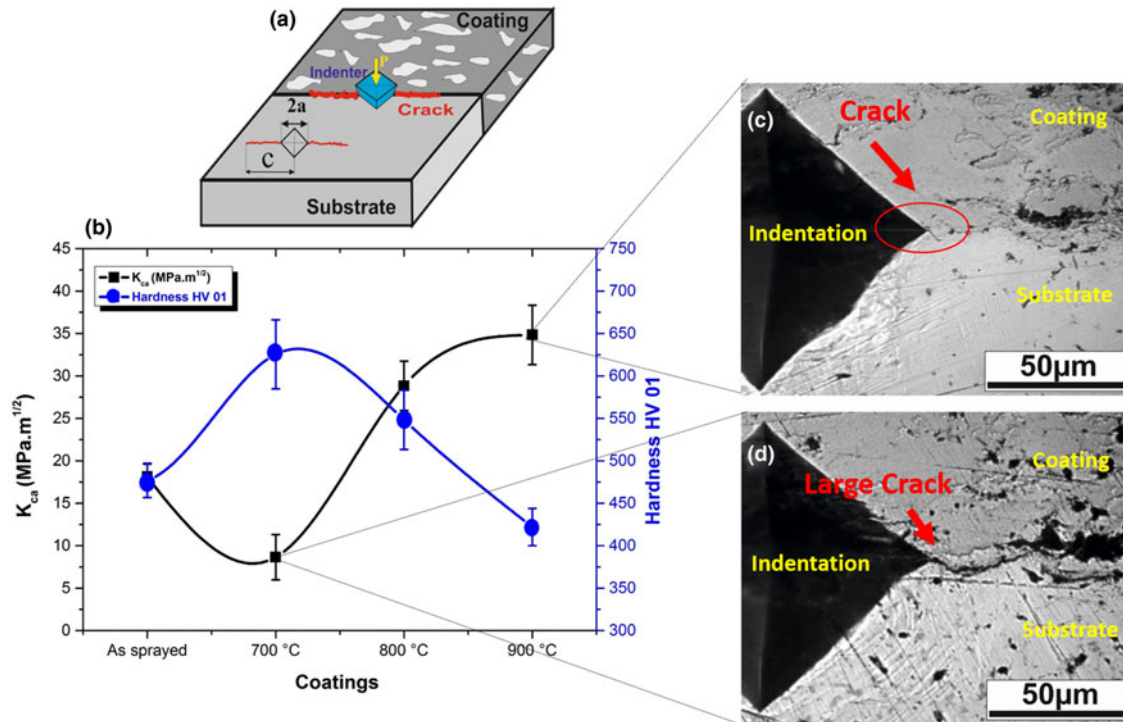
Figure 5: (a) Fundamental principle of the interfacial indentation test. (b) Comparison of the interfacial fracture toughness and hardness values. Optical images of coatings annealed at (c) 900 °C and (d) 700 °C, respectively.

induced by the thermal spray process and the carbide formation that is responsible for the metallic matrix hardening. This resulted in a larger deformation of the Vickers indent allowing for the delamination of the coating resulting in a more pronounced crack growth. However, samples annealed at 900 °C exhibited the largest K_{IC} values due to their relatively low hardness as well as the elasto-plasticity ratio of their metallic matrix that inhibited crack propagation at the substrate-coating interface.

Friction and wear behavior

The SEM observations of the worn surfaces of the as-sprayed and annealed samples are shown in Figs. 6(a)–6(d). All surfaces were characterized by local plastic deformation of the metallic matrix, scratches on the WC particles accompanied with some carbides fractured and removal of WC microparticles due to the porosity presence that plays an important role in the wear resistance of the coating. This porosity results in fracture and fatigue wear mechanism processes of the WC particles and micromachining (microcutting) of the metallic matrix during sliding test. The low hardness of the metallic matrix compared to the WC particles and the Al_2O_3 counter body resulted in abrasive wear and detachment of some parts of the matrix due to severe plastic deformation. Figure 6(b) suggests that the extent of plastic deformation is less pronounced for the

coatings that were annealed at 700 °C. Some cracks and scratches were observed and were attributed to the increase in the content of the hard phases. Grooves parallel to the sliding direction were observed in the area of the wear track in Figs. 6(c) and 6(d). These formed as a result of the sliding of hard particle debris trapped between the sample surface and the Al_2O_3 counter body. EDS point analysis measured in the worn surfaces (A, B, C, D, E, and F) and shown in Table 3 indicated that no counterpart elements were transferred to the wear track. Shallow plowing grooves combined with an abrasive type of wear was observed on the worn surfaces for the coatings annealed at 800 °C [Fig. 6(c)]. EDS analysis revealed the presence of some counterpart elements (Al and O), suggesting that the wear mechanism appears to be a combination of an abrasive and oxidative wear. Similar behavior was observed for the worn surface of the coatings annealed at 900 °C [Fig. 6(d)]. In this case, delamination of the WC particles and more abrasive damage and cracks were seen along the WC particles/metallic matrix interface. This indicates the poorer cohesion between the WC particles and the metallic matrix in the coatings annealed at 900 °C. This may be due to the more pronounced phase changes, discussed above, that occur as a result of the annealing process.

Figure 6(e) shows the coefficient of friction (CoF) data for as-sprayed and annealed samples. All of the curves exhibited the same initial run-in tendency and reached a steady state
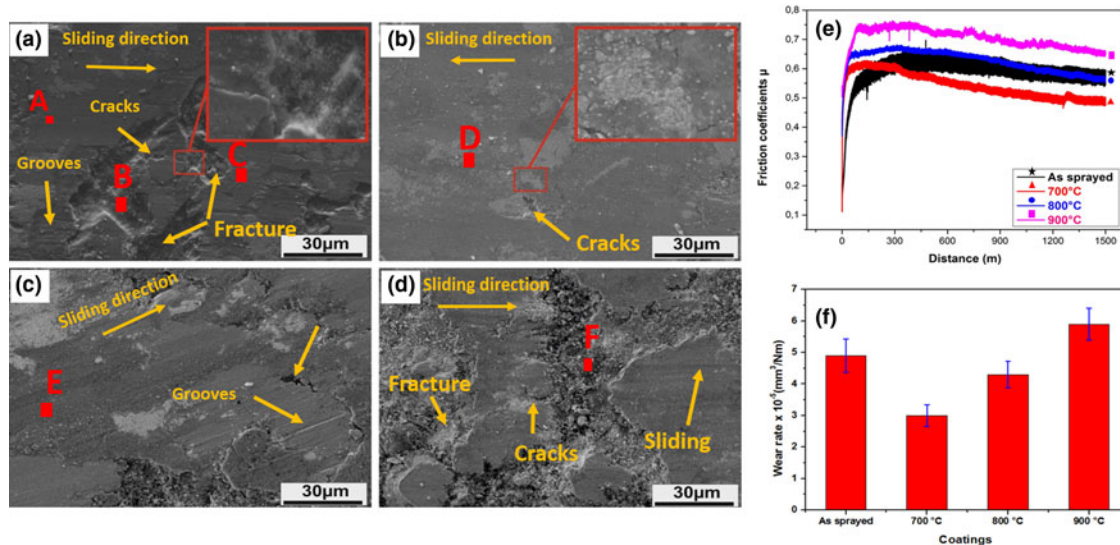
Figure 6: SEM micrograph showing the wear track of (a) as-sprayed and annealed coatings at (b) 700 °C, (c) 800 °C, and (d) 900 °C. (e) Friction coefficient data during tribotesting under a load of 15 N and a sliding distance of 1500 m. (f) Histogram showing the wear rate for pre- and post-annealed samples.

TABLE 3: EDS analyses of worm surfaces in zones A, B, C, D, E, and F shown in Fig. 6.

Powders (wt%)	W	Ni	Cr	Co	C	Fe	O	Al
A	07.45	74.93	15.47	–	–	02.15	–	–
B	25.26	61.81	09.51	–	–	03.27	–	–
C	84.08	04.12	03.94	07.86	–	–	–	–
D	70.73	13.21	6.47	07.16	–	–	02.43	–
E	14.78	42.03	10.01	02.74	–	–	24.90	03.50
F	13.24	43.02	09.89	02.17	02.86	02.46	22.69	03.67

Figure 7: Polar diagrams providing a visualization of different results (hardness, Young's modulus, wear rate, friction coefficient, and fracture toughness) for the coatings investigated in this study.

after about 300 m of sliding. The CoF values varied from 0.50 to 0.68 when the annealing temperature increased from 700 to 900 °C. The relatively larger CoF values for the NiCr–WC–Co coatings annealed at 900 °C was attributed to a decrease in coating hardness (see Fig. 5) [4]. Furthermore, the lowest CoF values were measured for samples annealed at 700 °C. This behavior is attributed to the relatively larger hardness values for these samples and the formation of a lubricious oxide tribolayer [34, 35]. It is worth mentioning that despite its high hardness, the 800 °C annealed coating exhibited a similar CoF to the as-sprayed one. It has been demonstrated that the hardness to modulus ratio (H/E) values, the so-called plasticity index, was shown to be a more appropriate parameter for the prediction of the wear behavior than the hardness alone [36]. In this study, there is no significant difference (around 0.06) between the H/E values for the as-sprayed and annealed coatings at different temperatures (Table 2). This indicates that the limit of elastic behavior is similar for all coatings [37]. The specific wear rates of the as-sprayed and annealed coatings are summarized in Fig. 6(f). As expected, the higher hardness leads to a lower wear rate. For the coatings annealed at 700 °C, the hardness reached maximum values of 625 ± 30 and the CoF
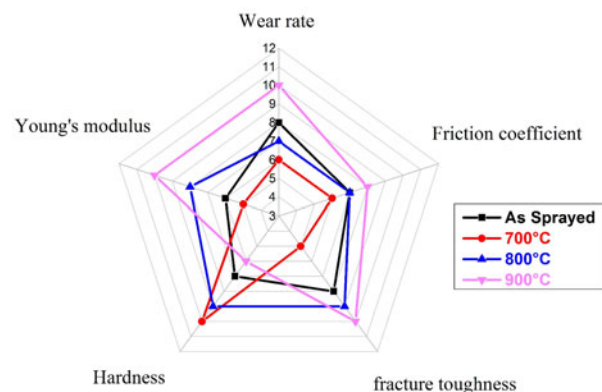
minimum values of 0.5. The wear rate was improved and reached values of $\sim 3 \times 10^{-5}$ mm³/nm compared to the as-sprayed coatings (5×10^{-5} mm³/Nm). The wear rate increased to 4×10^{-5} and 6×10^{-5} mm³/Nm for samples annealed at 800 and 900 °C, respectively. It is clear that with an increase in the annealing temperature, the thermal softening of the coating became more prominent and the increase in the wear rate from 700 to 900 °C annealing temperature was a result of their softening as well as to the increasing in the friction coefficient during sliding. Hence, samples annealed at 700 °C displayed the best wear conditions and this may be attributed to the metallic matrix strengthening, the higher volume fraction the WC particles, and the toughness of the metallic matrix–WC particles interface.

Figure 7 shows a polar diagram summarizing different mechanical and tribological properties for the coatings that

were investigated in this study. This diagram suggested that coatings annealed at 700 °C displayed the lowest wear rate and largest hardness values but have a low interfacial fracture toughness. On the other hand, coatings annealed at 900 °C showed the highest Young's modulus and interfacial fracture toughness but had a relatively larger wear rate. The pentagram areas for coating annealed at 800 °C consistently showed desirable values for all five categories. Hence, this diagram provides insights useful for developing NiCr–WC10Co MMCs coatings using the HVOF method followed by a heat-treatment process and that display tunable properties depending on the intended applications.

Conclusion

In the present work, the effect of annealing temperature on the microstructure, mechanical, and tribological properties of HVOF-produced NiCr–WC–Co coatings were studied. The following conclusions may be drawn:

(i) Higher annealing temperatures lead to a greater WC particle decarburization. This particle dissolution is accompanied by an increase in the amount of newly formed carbides (W_2C and Cr_3C_2).

(ii) The present study clearly suggests the annealing of NiCr–WC–Co HVOF-sprayed coating to 800 °C where an increase of 17% in hardness and Young's modulus of the coating is recorded with relatively low wear rate compared to the as-sprayed condition. The optimum annealing temperature is subject to substrate metallurgy and fatigue/creep resistance requirements.

(iii) The substrate/coating fracture toughness and adhesion is the highest for annealing temperatures of 900 °C.

(iv) SEM and EDS analyses indicated that the wear mechanism appeared to be abrasive for the as-sprayed coatings and was a combination of an abrasive and oxidative wear with increasing the annealing temperature.

(v) Coatings annealed at 800 °C displayed the best microstructure–mechanical properties–tribological performance balance as shown in the polar diagram presented in Fig. 7.

Materials and Methods

The substrate material that was selected for this study was 304 L austenitic stainless steel with low carbon content (<0.03 wt%) since it is widely used in various aggressive environments due to its excellent corrosion resistance. Coatings were created by an atomization process using a mixture of NiCr and WC–10%Co–4%Cr powders that had an average diameter of 30 ± 10 μm (Wisdom Company, Shanghai,

China). The nominal chemical composition (wt%) of the two powders was 77.0 ± 0.5% Ni and 23.0 ± 0.5% Cr for the NiCr powders and 89.9 ± 0.5% W, 7.3 ± 0.6% Co, and 2.8 ± 0.4% Cr for the WC10Co4Cr powders. The NiCr and WC–10% Co4%Cr powders were mixed in a stainless steel ball milling jar for 1 h in an argon atmosphere at room temperature using a rotational speed of 150 rpm to form a 60%NiCr 40% WC10Co4Cr composite. The shape of the powders did not change as a result of the mixing. The confirmation of nominal chemical compositions of the steel substrate and the powders is given by EDS analyses. The mixed powders were sprayed onto 304 L steel substrates using the HVOF process with the essential processing parameters that are summarized as follows: Fuel GPL; spray distance: 180 mm; oxygen flow rate: 500–600 L/min; and powder feed: 25–38 gm/min.

The coated samples were annealed using a heating rate of 5 °C/min in an electrical MAGMA muffle furnace at three different temperatures (700, 800, and 900 °C) for a 2-h holding time and were then cooled in air. These annealing temperatures were selected based on the surface temperatures reached under the working conditions in drilling tools.

XRD was performed using a Philips diffractometer, with 40 kV, Cu K_α radiation = 0.15406 nm and 0.05°/s step size. The recorded XRD patterns were characterized using a PANalytical X'Pert High Score software. An Ikon optical microscope and a JSM 6830 scanning electronic microscope were used to analyze the topography and microstructure. The SEM is equipped with an EDS module for elemental mapping. These characterization techniques were used to analyze as-sprayed and annealed samples.

Nano-indentation measurements were carried out using an Anton Paar NHT-3 nanoindenter with a Berkovich tip using a 100 mN applied load. The test was performed in selected areas of the coatings that include the metallic matrix, the metallic matrix–carbide interface, and the WC particles. Hardness and Young' modulus values were obtained for an average value of three tests conducted at different locations. Microhardness measurements were carried out using a Wilson HV3300 hardness tester under load of 10 N (HV 01) and 10 s dwell time. Interfacial fracture toughness values were estimated using the cohesion energy of the coatings based on Vickers indents performed with a 50 N (HV 5) applied load and a 15 s holding time [38, 39], as shown in Fig. 5(a). The apparent interfacial fracture toughness K_{ca} (MPa m$^{1/2}$) is calculated based on Evans' theory [40, 41]:

$$K_{ca} = 0.079 \times 10^3 \frac{P}{a^{3/2}} \, \text{Log} \, \frac{4.5 \, a}{c} \cdot \left(\frac{E}{H}\right)_I^{1/2}, \quad (1)$$

where P is the applied load (50 N), a is the half diagonal of the indentation (μm), and c is the crack length (μm).

The ratio $(E/H)_I$ in the above equation is defined by [42, 43]:

$$\left(\frac{E}{H}\right)_I^{1/2} = \frac{(E/H)_S^{1/2}}{1 + (H_S/H_C)^{1/2}} + \frac{(E/H)_C^{1/2}}{1 + (H_C/H_S)^{1/2}}, \quad (2)$$

where E is the Young modulus (GPa), H is the hardness (GPa), S, C, and I refer to the substrate, the coating, and the interface, respectively.

Tribological tests were carried out using a ball-on-disk tribometer (CSM Instruments Inc, Peseux, Switzerland), based on the ASTM G99-0516 standard. The tribotests were performed at a constant velocity of 15 cm/s and an applied normal load of 15 N for sliding distances of 1500 m. A 6 mm Al_2O_3 ball was selected as the counter body. All tests were conducted at room temperature under dry laboratory conditions. The width, d, of the wear track was determined with a 2D profilometer equipped with profiler software to determine the cross-sectional area of the sliding track. During sliding, the friction coefficient was continuously measured and recorded in real time by TriboX. At the end of each test, the friction coefficient μ curves were determined and the wear rate W_s for each specimen are calculated using the following equation:

$$W_s = \frac{V_{disk}}{D_s F}, \quad (3)$$

where D_s is the sliding distance (m), V_{disk} is the disc volume loss, and F (N) is the applied load.

Acknowledgments

References

1. M. Magnani, P.H. Suegama, N. Espallargas, S. Dosta, C.S. Fugivara, J.M. Guilemany, and A.V. Benedetti: Influence of HVOF parameters on the corrosion and wear resistance of WC-Co coatings sprayed on AA7050 T7. *Surf. Coat. Technol.* **202**, 4746–4757 (2008).

2. M. Jafari, J.C. Han, J.B. Seol, and C.G. Park: Tribological properties of HVOF-sprayed WC-Co coatings deposited from Ni-plated powders at elevated temperature. *Surf. Coat. Technol.* **327**, 48–58 (2017).

3. C. Zheng, Y. Liu, J. Qin, C. Chen, and R. Ji: Wear behavior of HVOF sprayed WC coating under water-in-oil fracturing fluid condition. *Tribol. Int.* **115**, 28–34 (2017).

4. T.B. Torgerson, M.D. Harris, S.A. Alidokht, T.W. Scharf, S.M. Aouadi, R.R. Chromik, J.S. Zabinski, and A.A. Voevodin: Room and elevated temperature sliding wear behavior of cold sprayed Ni-WC composite coatings. *Surf. Coat. Technol.* **350**, 136–145 (2018).

5. M. Richert and B.M. Leszczyńska: Effect of the annealing on the microstructure of HVOF deposited coatings. *J. Achiev. Mater. Manuf. Eng.* **46**, 95–102 (2011).

6. B. Li, X. Wang, H. Chen, J. Hu, C. Huang, and G. Gou: Influence of heat treatment on the strength and fracture toughness of 7N01 aluminum alloy. *J. Alloys Compd.* **678**, 160–166 (2016).

7. M. Tocci, R. Donnini, G. Angella, and A. Pola: Effect of Cr and Mn addition and heat treatment on $AlSi_3Mg$ casting alloy. *Mater. Charact.* **123**, 75–82 (2017).

8. M. Dehestani, K. Trumble, H. Wang, H. Wang, and L.A. Stanciu: Effects of microstructure and heat treatment on mechanical properties and corrosion behavior of powder metallurgy derived Fe–30Mn alloy. *Mat. Sci. Eng.* **703**, 214–226 (2017).

9. Š. Houdková, E. Smazalová, M. Vostřák and M. Vostřák: Properties of NiCrBSi coating, as sprayed and remelted by different technologies. *Surf. Coat. Technol.* **253**, 14-26 (2014).

10. M-S. Yanga, X-B. Liua, J-W. Fanb, X-M. Hea, S-H. Shi, G-Y. Fua, M-D. Wanga, and S-F. Chenc: Microstructure and wear behaviors of laser clad NiCr/Cr3C2–WS2 high temperature self-lubricating wear-resistant composite coating. *Appl. Surf. Sci.* **258**, 3757–3762 (2012).

11. S. Zhou, X. Zeng, Q. Hu, and Y. Huang: Analysis of crack behavior for Ni-based WC composite coatings by laser cladding and crack-free realization. *Appl. Surf. Sci.* **255**, 1646–1653 (2008).

12. L. Janka, J. Norpoth, R. Trache, and L.M. Berger: Influence of heat treatment on the abrasive wear resistance of a Cr_3C_2NiCr coating deposited by an ethene-fuelled HVOF spray process. *Surf. Coat. Technol.* **291**, 444–451 (2016).

13. S. Houdková, E. Smazalová, and Z. Pala: Effect of heat treatment on the microstructure and properties of HVOF-sprayed Co-Cr-W coating. *J. Thermal Spray Technol.* **25**, 546–557 (2016).

14. A. Belamri, A. Ati, M. Braccini, and S. Azem: Hypereutectoid steel coatings obtained by thermal flame spraying — Effect of annealing on microstructure, tribological properties and adhesion energy. *Surf. Coat. Technol.* **263**, 86–99 (2016).

15. Y. Guo, Q. Liu, and X. Shang: Investigation on annealing strengthening effect of laser cladding Fe5Cr5Co5SiTiNbMoW high-entropy alloy coating. *J. Mater. Res.* **33**, 3339–3346 (2018).

16. L. Liu, H. Xu, J. Xiao, X. Wei, G. Zhang, and C. Zhang: Effect of heat treatment on structure and property evolutions of atmospheric plasma sprayed NiCrBSi coatings. *Surf. Coat. Technol.* **325**, 548–554 (2017).

17. Z. Bergant, U. Trdan, and J. Grum: Effect of high-temperature furnace treatment on the microstructure and corrosion behavior of NiCrBSi flame-sprayed coatings. *Corros. Sci.* **88**, 372–386 (2014).

18. **Z. Bergant and J. Grum**: Quality improvement of flame sprayed, heat treated, and remelted NiCrBSi coatings. *J. Thermal Spray Technol.* **18**, 380–391 (2009).

19. **X-L. Lua, X-B. Liua, P-C. Yua, Y-J. Zhai, S-J. Qiaoa, M-D. Wanga, Y-G. Wanga, and Y. Chena**: Effects of heat treatment on microstructure and mechanical properties of Ni60/h-BN self-lubricating anti-wear composite coatings on 304 stainless steel by laser cladding. *Appl. Surf. Sci.* **355**, 350–358 (2015).

20. **D.A. Stewart, P.H. Shipway, and D.G. McCartney**: Influence of heat treatment on the abrasive wear behaviour of HVOF sprayed WC–Co coatings. *Surf. Coat. Technol.* **105**, 13–24 (1998).

21. **S.K. Asl, M.H. Sohi, K. Hokamoto, and M. Uemura**: Effect of heat treatment on wear behavior of HVOF thermally sprayed WC-Co coatings. *Wear* **260**, 1203–1208 (2006).

22. **T. Wang and F. Ye**: The elevated-temperature wear behavior evolution of HVOF sprayed tungsten carbide coatings: Respond to heat treatment. *Internat. J. Refract. Metals Hard Mater.* **71**, 92–100 (2018).

23. **J-K.N. Murthy, S. Bysakh, K. Gopinath, and B. Venkataraman**: Microstructure dependent erosion in Cr3C2–20 (NiCr) coating deposited by a detonation gun. *Surf. Coat. Technol.* **202**, 1–12 (2007).

24. **J-K.N. Murthy, K.S. Prasad, K. Gopinath, and B. Venkataraman**: Characterisation of HVOF sprayed Cr3C2-50 (Ni20Cr) coating and the influence of binder properties on solid particle erosion behaviour. *Surf. Coat. Technol.* **204**, 3975–3985 (2010).

25. **A.C. Karaoglanli, H. Caliskan, M. Oge, K.M. Doleker, and M. Hotamis**: Comparison of tribological properties of HVOF sprayed coatings with different composition. *Surf. Coat. Technol.* **318**, 299–308 (2017).

26. **Z. Geng, S. Li, D-L. Duan, and Y. Liu**: Wear behaviour of WC–Co HVOF coatings at different temperatures in air and argon. *Wear* **330**, 348–353 (2015).

27. **A-J. Gant, J-W. Nunn, M-G. Gee, D. Gorman, D.D. Gohil, and L.P. Orkney**: New perspectives in hardmetal abrasion simulation. *Wear* **376**, 2–14 (2017).

28. **T. Liyanage, G. Fisher, and A. Gerlich**: Microstructures and abrasive wear performance of PTAW deposited Ni–WC overlays using different Ni-alloy chemistries. *Wear* **274**, 345–354 (2012).

29. **B. Cheniti, D. Miroud, P. Hvizdoš, J. Balko, R. Sedlák, T. Csanádi, B. Belkessa, and M. Fides**: Investigation of WC decarburization effect on the microstructure and wear behavior of WC-Ni hardfacing under dry and alkaline wet conditions. *Mater. Chem. Phys.* **208**, 237–247 (2018).

30. **M.J. Tobar, C. Álvarez, J-M. Amado, G. Rodríguez, and A. Yáñez**: Morphology and characterization of laser clad composite NiCrBSi–WC coatings on stainless steel. *Surf. Coat. Technol.* **200**, 6313–6317 (2006).

31. **S-Y. Ahn and S. Kang**: Formation of core/rim structures in Ti (C, N)-WC-Ni cermets via a dissolution and precipitation process. *J. Am. Ceram. Soc.* **83**, 1489–1494 (2000).

32. **M. Tang, Y. Du, P. Zhou, S. Wang, H. Zhang, Y. Zeng, S. Liu, X. Chai, Y. Peng, C. Wu, X. Su, and Z-K. Liu**: Experimental phase diagram, thermodynamic modeling and solidified microstructure in the Mo–Ni–W ternary system. *Calphad* **68**, 101748 (2020).

33. **W.C. Oliver and G.M. Pharr**: An improved technique for determining hardness and elastic modulus using load and displacement sensing indentation experiments. *J. Mater. Res.* **7**, 1564–1583 (1992).

34. **Y. Zhang, Y. Epshteyn, and R.R. Chromik**: Dry sliding wear behaviour of cold-sprayed Cu-MoS$_2$ and Cu-MoS$_2$-WC composite coatings: the influence of WC. *Tribol. Int.* **123**, 296–306 (2018).

35. **F.H. Stott and G.C. Wood**: The influence of oxides on the friction and wear of alloys. *Tribol. Int.* **11**, 211–218 (1978).

36. **A. Leyland and A. Matthews**: On the significance of the H/E ratio in wear control: A nanocomposite coating approach to optimised tribological behaviour. *Wear* **246**, 1–11 (2000).

37. **S.M. Aouadi, J. Gu, and D. Berman**: Self-healing ceramic coatings that operate in extreme environments: A review. *J. Vac. Sci. Technol. A* **38**, 050802 (2020).

38. **J. Lesage and D. Chicot**: Role of residual stresses on interface toughness of thermally sprayed coatings. *Thin Solid Films* **415**, 143–150 (2002).

39. **G. Marot, P. Démarécaux, J. Lesage, M. Hadad, S. Siegmann, and M.H. Staia**: The interfacial indentation test to determine adhesion and residual stresses in NiCr VPS coatings. *Surf. Coat. Technol.* **202**, 4411–4416 (2008).

40. **A.G. Evans and E.A. Charles**: Fracture toughness determinations by indentation. *J. Am. Ceram. Soc.* **59**, 371–372 (1976).

41. **P. Zhang and Z. Liu**: Effect of sequential turning and burnishing on the surface integrity of Cr–Ni-based stainless steel formed by laser cladding process. *Surf. Coat. Technol.* **276**, 327–335 (2015).

42. **Y. Yamazaki, M. Arai, Y. Miyashita, H. Waki, and M. Suzuki**: Determination of interfacial fracture toughness of thermal spray coatings by indentation. *J. Thermal Spray Technol.* **22**, 1358–1365 (2013).

43. **J. Lesage, M-H. Staia, D. Chicot, C. Godoy, and P.E.V. De Miranda**: Effect of thermal treatments on adhesive properties of a NiCr thermal sprayed coating. *Thin Solid Films* **377**, 681–686 (2000).